Enhanced reversibility of the magnetoelastic transition in $(Mn,Fe)_2(P,Si)$ alloys via minimizing the transition-induced elastic strain energy

Miao, Xuefei; Gong, Yong; Zhang, Fengqi; You, Yurong; Caron, Luana; Qian, Fengjiao; Xu, Feng; van Dijk, Niels; Brück, Ekkes; More Authors

DOI
10.1016/j.jmst.2021.05.087

Publication date
2022

Document Version
Final published version

Published in
Journal of Materials Science and Technology

Journal of Materials Science & Technology 103 (2022) 165–176

Contents lists available at ScienceDirect

Journal of Materials Science & Technology

journal homepage: www.elsevier.com/locate/jmst

Research Article

Enhanced reversibility of the magnetoelastic transition in $(Mn,Fe)_2(P,Si)$ alloys via minimizing the transition-induced elastic strain energy

Xuefei Miao[a,*], Yong Gong[a], Fengqi Zhang[b], Yurong You[a], Luana Caron[c,d], Fengjiao Qian[e], Wenhui Guo[a], Yujing Zhang[a], Yuanyuan Gong[a], Feng Xu[a,*], Niels van Dijk[b], Ekkes Brück[b]

[a] MIIT Key Laboratory of Advanced Metallic and Intermetallic Materials Technology, School of Materials Science and Engineering, Nanjing University of Science and Technology, Nanjing 210094, China
[b] Fundamental Aspects of Materials and Energy, Department of Radiation Science and Technology, Delft University of Technology, Mekelweg 15, Delft, JB 2629, Netherlands
[c] Department of Physics, Bielefeld University, Bielefeld 33501, Germany
[d] Helmholtz-Zentrum Berlin für Materialien und Energie, Berlin 12489, Germany
[e] College of Physics, Nanjing University of Aeronautics and Astronautics, Nanjing 210016, China

ARTICLE INFO

Article history:
Received 18 April 2021
Revised 10 May 2021
Accepted 11 May 2021

Keywords:
Magnetocaloric effect
$(Mn,Fe)_2(P,Si)$
Hysteresis
Neutron diffraction

ABSTRACT

Magnetocaloric materials undergoing reversible phase transitions are highly desirable for magnetic refrigeration applications. $(Mn,Fe)_2(P,Si)$ alloys exhibit a giant magnetocaloric effect accompanied by a magnetoelastic transition, while the noticeable irreversibility causes drastic degradation of the magnetocaloric properties during consecutive cooling cycles. In the present work, we performed a comprehensive study on the magnetoelastic transition of the $(Mn,Fe)_2(P,Si)$ alloys by high-resolution transmission electron microscopy, *in situ* field- and temperature-dependent neutron powder diffraction as well as density functional theory calculations (DFT). We found a generalized relationship between the thermal hysteresis and the transition-induced elastic strain energy for the $(Mn,Fe)_2(P,Si)$ family. The thermal hysteresis was greatly reduced from 11 to 1 K by a mere 4 at.% substitution of Fe by Mo in the $Mn_{1.15}Fe_{0.80}P_{0.45}Si_{0.55}$ alloy. This reduction is found to be due to a strong reduction in the transition-induced elastic strain energy. The significantly enhanced reversibility of the magnetoelastic transition leads to a remarkable improvement of the reversible magnetocaloric properties, compared to the parent alloy. Based on the DFT calculations and the neutron diffraction experiments, we also elucidated the underlying mechanism of the tunable transition temperature for the $(Mn,Fe)_2(P,Si)$ family, which can essentially be attributed to the strong competition between the covalent bonding and the ferromagnetic exchange coupling. The present work provides not only a new strategy to improve the reversibility of a first-order magnetic transition but also essential insight into the electron-spin-lattice coupling in giant magnetocaloric materials.

1. Introduction

The magnetocaloric effect (MCE) couples a change in the magnetic field to a change in temperature of the material and thereby lays the foundation for magnetic refrigeration, a cutting-edge cooling technology with merits of high energy efficiency and low environmental impact [1,2]. A giant MCE is usually accompanied by first-order magnetic transitions (FOMTs), as observed in $Gd_5(Si,Ge)_4$ [3], $(Mn,Fe)_2(P,Si)$ [4], $La(Fe,Si)_{13}$ [5,6], MnMX [7,8] and NiMn-based Heusler alloys [9,10]. The FOMT is tied to either a structural transformation (*i.e.* magnetostructural transition) or to discontinuous changes in the unit-cell parameters with a conserved symmetry of the lattice (*i.e.*, magnetoelastic transition). Therefore, a concrete strategy for seeking giant MCE materials is to screen materials with magnetostructural or magnetoelastic transitions. Nevertheless, the irreversibility of the magnetostructural or magnetoelastic transitions, manifesting itself in thermal and magnetic hysteresis, causes a drastic reduction of the MCE during consecutive cooling cycles [11,12]. Consequently, understanding and eliminating this hysteresis is crucial for the commercialization of this revolutionary cooling technology.

According to Landau theory [13–15], several local minima are present in the Gibbs free energy of a FOMT system in the vicinity of the transition. The selected local minimum depends on the thermal and field history of the system. As a result, the FOMT

* Corresponding authors.
E-mail addresses: xuefeimiao@njust.edu.cn (X. Miao), xufeng@njust.edu.cn (F. Xu).

https://doi.org/10.1016/j.jmst.2021.05.087
1005-0302/

is controlled by different energy barriers between the local and global minima in the Gibbs free energy during cooling and heating (or increasing and decreasing the magnetic field), which causes thermal (or magnetic) hysteresis. Apart from this intrinsic hysteresis, structural defects like dislocations, second-phase particles and micro-cracks may also affect the reversibility of a FOMT [16–18]. Structural defects may locally facilitate the nucleation of the new phase (heterogeneous nucleation), resulting in a reduction of the hysteresis, or may cause pinning of the moving interface during the growth of the new phase, increasing the hysteresis (extrinsic hysteresis).

Different ways of minimizing the hysteresis have been proposed, which can be separated into five main categories: (i) tailoring the order of the transition [19–21]; (ii) improving the structural compatibility between phases [22–27]; (iii) introducing nano-precipitations or multi-scale structural defects [28–38]; (iv) tuning the kinetics of the transition [39,40]; (v) driving the transition via multi-stimuli [10,41]. Unlike first-order phase transitions, second-order phase transitions are completely reversible and present no hysteresis, although the MCE is moderate. A balance between the MCE and the reversibility can be achieved by tuning the transition towards the tricritical point, *i.e.* the crossover from first to second order. At the tricritical point, materials exhibit no hysteresis but retain a giant MCE, as demonstrated in the MnCo(Ge,Si) [19] and Tb_5SiGe_2 [20] alloys. As revealed by *in situ* neutron diffraction [42] and Hall-probe imaging measurements [19], the first-order magnetic transition is driven by the nucleation and growth of the product phase from the parent phase. It has been found that the NiTi-based shape memory alloys [23], NiMn-based Heusler alloys [24–26] and MnNiGe-based alloys [27] exhibit low hysteresis when the product and the parent phases satisfy certain geometric compatibility conditions. In addition, the presence of nano-precipitations [28–31], local atomic disorder [32–34] and nano-pores [35] has also been proven to lower the nucleation barrier and reduce the hysteresis. At the mesoscopic scale, the partial removal of grain boundaries [36] and the introduction of micro-cracks [37] or micro-pores [38] can also lead to smaller hysteresis since the transition-induced stress is easier to be released. Apart from tuning the giant MCE material itself, the hysteresis can finally be reduced by optimizing the external stimuli, *e.g.*, a small sweeping rate of the driving field [39,40] and the utilization of multicaloric cycles driven by magnetic-pressure [10] or magnetic-electric [41] multi-stimuli.

Extensive studies have been carried out to reduce the hysteresis of the $(Mn,Fe)_2(P,Si)$ alloys that show great application potential due to the giant MCE and the abundance of the constituent elements. Without understanding the underlying mechanism causing the hysteresis, the development of superior $(Mn,Fe)_2(P,Si)$ alloys is largely based on trial and error. In the present work, we employed a high-resolution transmission electron microscope (TEM), *in situ* field- and temperature-dependent neutron powder diffraction (NPD) as well as density functional theory calculations (DFT) to explore the first-order magnetoelastic transition in the $(Mn,Fe)_2(P,Si)$ alloys. We found a generalized relationship between the thermal hysteresis and the transition-induced elastic strain energy for the $(Mn,Fe)_2(P,Si)$ family, which offers new guidance for optimizing this material system and other giant MCE materials.

2. Experimental details

2.1. Sample synthesis

$Mn_{1.15}Fe_{0.80-x}Mo_xP_{0.45}Si_{0.55}$ (x = 0, 0.01, 0.02 and 0.04) polycrystalline alloys were prepared by high-energy ball milling from Mn, Fe, Mo, red P and Si powders (purity better than 99.8 wt.%). The off-stoichiometry of the nominal compositions, *i.e.* slight deficiency in the metal elements, was intended to reduce the Fe_3Si-type secondary phase [17,43]. The fine powders after ball milling were pressed into tablets at room temperature, sealed into quartz ampoules in vacuum and sintered at 1373 K for 40 h. The samples were quenched into iced water after sintering.

2.2. Crystal and magnetic structure characterization

Neutron powder diffraction measurements were performed on the high-intensity powder diffractometer (WOMBAT) [44] at the OPAL Reactor (Lucas Heights, Australia). The $Mn_{1.15}Fe_{0.80-x}Mo_xP_{0.45}Si_{0.55}$ powders were loaded into a vanadium can and subsequently fixed with aluminum foils. For temperature-dependent measurements in zero field, a top loading cryofurnace was used and the data were collected between 4 and 350 K upon warming. For magnetic field-dependent measurements, a vertical field magnet was used, which can provide magnetic fields up to 9 T between 1.5 and 300 K. To avoid any temperature- or field-history effect on the field-dependent measurements, the samples were always zero-field cooled from 300 K to the specific measuring temperature before starting the field-dependent measurements. The incident neutron wavelength was 1.542047 and 2.410418 Å for the temperature- and field-dependent measurements, respectively.

Temperature-dependent X-ray powder diffraction (XRD) measurements were performed on a PANalytical X-pert Pro-diffractometer with a low-temperature chamber (Anton Paar TTK450). Crystallographic and magnetic structure refinement of the NPD and XRD patterns was performed using Fullprof's [45] implementation of the Rietveld refinement method.

2.3. Microstructure observation and composition analysis

Surface morphology and compositional analysis of the samples were characterized using a field-emission scanning electron microscope (SEM, ZEISS, Sigma 500) equipped with an X-ray energy dispersive spectroscope (EDS).

Atomic-resolution structural characterization was performed on an FEI Titan Themis 80–300 transmission electron microscope, which is equipped with two (probe and image) aberration correctors and a highly efficient (4 quadrant) EDS. This TEM offers a maximum resolution of 0.06 nm in the high-angle annular dark-field (HAADF) scanning TEM (STEM) mode. The TEM specimen was prepared in a focused ion beam system (FIB, FEI, Helios Nanolab 600i) using the lift-out method.

2.4. Magnetic and calorimetric characterization

The magnetic properties were measured in a superconducting quantum interference device magnetometer (SQUID, Quantum Design MPMS 5XL) using the reciprocating sample option (RSO) mode. Reversible ΔT_{ad} of the $Mn_{1.15}Fe_{0.80-x}Mo_xP_{0.45}Si_{0.55}$ (x = 0, 0.01, 0.02 and 0.04) alloys was measured in a homemade device [46,47] at Delft University of Technology, the Netherlands. The powdered samples were compressed in a capsule. A Chromel-Constantan thermocouple was buried inside the powders to directly probe the temperature of the sample. During the measurement, the environment temperature was changed continuously between 240 and 310 K at a sweeping rate of 0.5–1.5 K min^{-1}. The sample was moved at a frequency of 0.1 Hz in and out of a magnetic field ($\mu_0 H$ = 1.1 T) generated by a permanent magnet. A temperature rise and drop was detected about every 10 s due to the field cycling. The thermal relaxation rate related to the MCE was about 150 K min^{-1}, much faster than the sweeping rate of the environment temperature and hence ensuring quasi-adiabatic conditions. The reversible ΔT_{ad} was determined as the reversible part of the temperature rise and drop accompanied by the magnetization

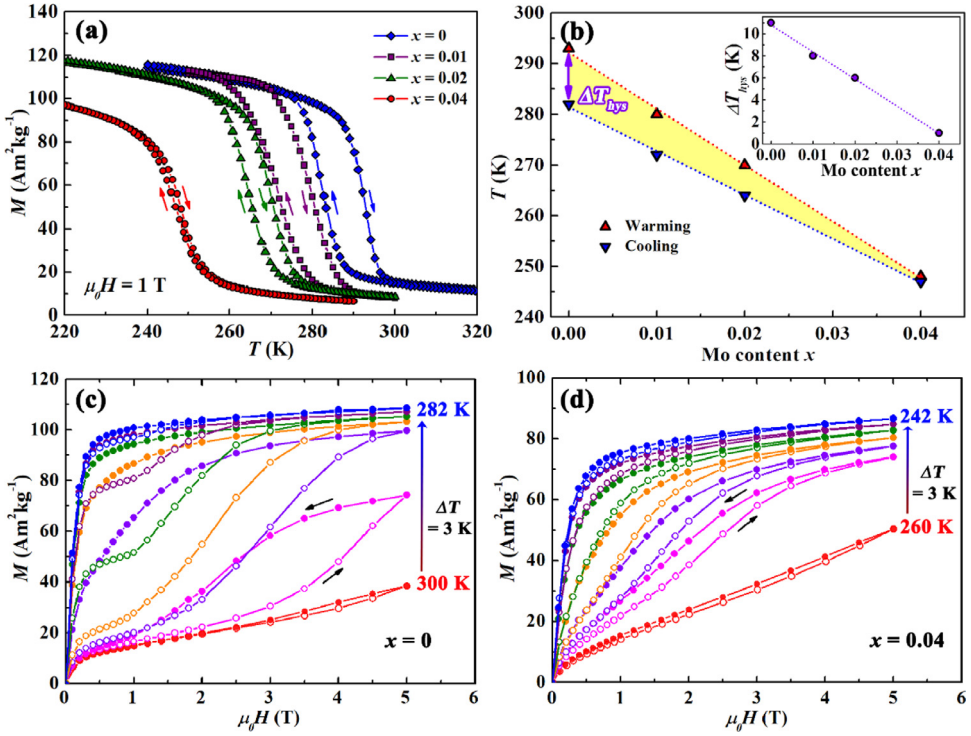

Fig. 1. (a) Temperature-dependent magnetization measured in 1 T for the $Mn_{1.15}Fe_{0.80-x}Mo_xP_{0.45}Si_{0.55}$ alloys. (b) Curie temperature as a function of the Mo content derived from the thermomagnetic curves. The dependence of thermal hysteresis on the Mo content is shown in the inset of (b). Isothermal magnetization/demagnetization curves for the $x = 0$ (c) and 0.04 (d) alloys.

and demagnetization of the magnetocaloric powders. The specific heat (C_p) at different temperatures was measured at a sweeping rate of 10 K min^{-1} in a commercial differential scanning calorimeter (DSC, TA Instrument Q2000).

2.5. Electronic structure calculations

Density functional theory calculations were performed on the $(Mn,Fe,Mo)_2(P,Si)$ alloys using the Vienna ab initio simulation package (VASP) [48]. Perdew-Burke-Ernzerhof (PBE) pseudopotentials with generalized gradient approximation (GGA) were implemented in exchange correlation functions. A plane-wave cutoff energy of 500 eV and a Γ-centered *k*-point mesh of 9 × 9 × 9 were taken. A 2 × 2 × 2 supercell was constructed, where one of the 24 Mn (or Fe) atoms at the 3 *g* (or 3*f*) sites was replaced by the Mo atom, corresponding to about 4% Mo substitution for the Mn or Fe in the $(Mn,Fe)_2(P,Si)$ alloys. The unit-cell parameters of the supercell were taken from the neutron diffraction results of the $Mn_{1.15}Fe_{0.76}Mo_{0.04}P_{0.45}Si_{0.55}$ sample measured at 5 K.

Electron localization function (ELF) [49], indicating the strength of chemical bonds between neighboring atoms, was calculated for the $(Mn,Fe)_2(P,Si)$ alloy in both paramagnetic (PM) and ferromagnetic (FM) states. The PM state was modeled by a 1 × 1 × 2 supercell, which is double the FM supercell with antiparallel moment ordering along *c* axis of the hexagonal structure to make the net moment zero. For simplicity, the 3 *g*, 3*f*, 2*c* and 1*b* sites in both supercells were fully occupied by the Mn, Fe, Si and P atoms, respectively.

3. Results and discussion

3.1. Magnetic properties

Fig. 1(a) shows the magnetization (M) measured at various temperatures (T) for the $Mn_{1.15}Fe_{0.80-x}Mo_xP_{0.45}Si_{0.55}$ alloys. The Curie temperature (T_C) of the magnetoelastic transition can be determined from the M–T curves, which corresponds to the temperature where the |dM/dT| shows a maximum. The T_C values of the cooling and warming branches for all the $Mn_{1.15}Fe_{0.80-x}Mo_xP_{0.45}Si_{0.55}$ alloys are plotted in Fig. 1(b). The Mo-free alloy shows a considerable difference in the T_C between the cooling and warming branches, indicating a large thermal hysteresis (ΔT_{hys}) of the magnetoelastic transition. By partial substitution of Fe by Mo, the T_C decreases almost linearly at a rate of 11.1(3) and 8.7(3) K/at.% Mo substitution for the warming and cooling branches, respectively. The faster decrease in the T_C of the warming branch than that of the cooling branch leads to a smaller ΔT_{hys} in the samples with higher Mo contents. ΔT_{hys} also shows a linear dependence on the Mo content (see the inset of Fig. 1(b)). The value of ΔT_{hys} is significantly reduced from 11 to 1 K (*i.e.* by about 91%) via a mere 4 at.% Mo substitution for Fe in the $Mn_{1.15}Fe_{0.80}P_{0.45}Si_{0.55}$ alloy.

Fig. 1(c) and (d) presents the isothermal magnetization/demagnetization curves measured at temperatures close to the T_C of the Mo-free and $x = 0.04$ alloys, respectively. The field-induced PM-to-FM transition can be observed in both alloys, manifested by the rapid increase in the magnetization above a critical magnetic field (*e.g.*, above 3 T in the M–H curve collected at 297 K for the Mo-free alloy shown in Fig. 1(c)). Both alloys display a magnetic hysteresis, which characterizes the irreversibility of the field-induced PM-to-FM transition. Nevertheless, the magnetic hysteresis is greatly reduced in the $x = 0.04$ alloy compared to the Mo-free alloy. Therefore, the $x = 0.04$ alloy shows both smaller thermal and magnetic hysteresis than the Mo-free alloy, suggesting enhanced reversibility of the magnetoelastic transition after Mo substitution.

3.2. In situ *field-dependent neutron diffraction studies*

We further performed *in situ* field-dependent neutron diffraction experiments to quantitatively study the reversibility of the

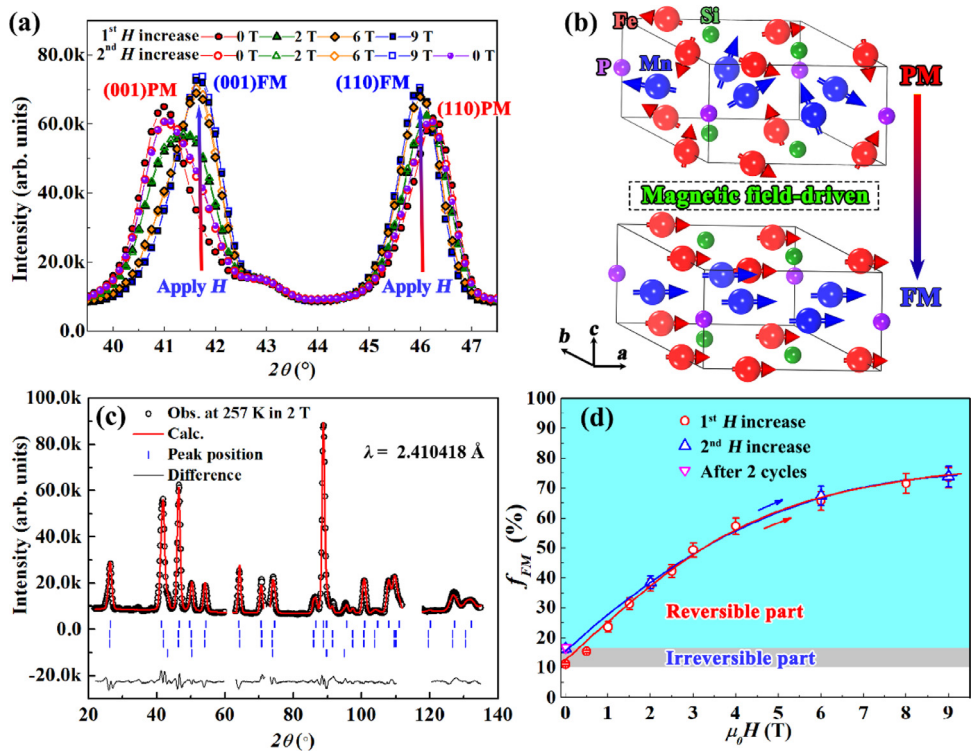

Fig. 2. (a) *In situ* field-dependent neutron diffraction patterns collected at 257 K from the $Mn_{1.15}Fe_{0.76}Mo_{0.04}P_{0.45}Si_{0.55}$ alloy. (b) Schematic illustration of the field-induced magnetoelastic transition in the $(Mn,Fe)_2(P,Si)$ alloys. (c) Rietveld refinement of the neutron diffraction pattern collected in 2 T at T = 257 K after zero-field cooling from 300 K. Vertical lines indicate the peak positions (from top to bottom) of the PM $(Mn,Fe)_2(P,Si)$ phase, the nuclear structure of the FM $(Mn,Fe)_2(P,Si)$ phase, the magnetic structure of the FM $(Mn,Fe)_2(P,Si)$ phase, and the Fe_3Si-type impurity phase, respectively. Note that the diffraction peaks from the magnet are excluded from the diffraction patterns. (d) The volume fraction of the transformed FM phase (f_{FM}) derived from neutron diffraction patterns during the first 2 field cycles at 257 K after zero-field cooling from 300 K. The solid lines in (d) are guided to the eyes.

magnetoelastic transition in the x = 0.04 alloy. Fig. 2(a) shows the neutron diffraction patterns collected at 257 K (slightly higher than T_C) from the x = 0.04 sample. The peaks at the 2θ of 41.0° and 46.2° in the zero-field diffraction pattern are indexed as the (001) and (110) Bragg peaks of the Fe_2P-type hexagonal structure, respectively. With increasing the magnetic field from 0 to 9 T, two new peaks centered at 41.6° and 46.0° appear and grow at the expense of the original peaks centered at 41.0° and 46.2°, respectively. According to the Rietveld refinement, the two new peaks also belong to the Fe_2P-type hexagonal structure, but with different lattice parameters. This reveals a magnetic field-driven magnetoelastic transition, where the PM-to-FM transition is coupled to discontinuous changes in the lattice parameters. Upon removal of the magnetic field, a slightly different diffraction pattern was obtained as compared to the original zero-field diffraction pattern, suggesting partial irreversibility of the magnetoelastic transition during the first field cycle. It should be noted that the irreversibility during the first field cycle is not due to the so-called "virgin effect" [17,18,50] since the sample was thermally cycled using liquid nitrogen before the field-dependent neutron diffraction measurements. When the magnetic field is applied for the second time, the diffraction patterns overlap with those collected at the same field during the first field cycle. Additionally, the zero-field diffraction patterns collected before and after the second field cycle are almost identical, suggesting complete reversibility of the magnetoelastic transition during the second field cycle.

The fraction of the transformed FM phase (f_{FM}) in different magnetic fields can be determined from the Rietveld refinement of the neutron diffraction patterns (see Fig. 2(c) as an example). Fig. 2(d) shows the evolution of the fraction of the FM phase with respect to the applied magnetic field. Note that a small amount (3.5 ± 0.2 wt.%) of the Fe_3Si-type impurity phase was detected in the $Mn_{1.15}Fe_{0.76}Mo_{0.04}P_{0.45}Si_{0.55}$ sample. The f_{FM} values shown in Fig. 2(d) correspond to the transformed fraction of the $(Mn,Fe)_2(P,Si)$ main phase. Upon cooling from 300 to 257 K in zero field, about 11.2% of the $Mn_{1.15}Fe_{0.76}Mo_{0.04}P_{0.45}Si_{0.55}$ alloy is in the FM state (*i.e.* $f_{FM} \approx$ 11.2%). With increasing the magnetic field, f_{FM} rises quickly and reaches approximately 73.6% at 9 T, manifesting a field-driven PM-to-FM transition. Upon removing the magnetic field, the inverse transition occurs and f_{FM} drops back to 16.4%. As a result, slightly more (about 5.3%) FM phase is present at zero field after the first field cycle, corresponding to the irreversible part of the transition. When applying the field for the second time, f_{FM} increases again and reaches roughly the same values at 2, 6 and 9 T as observed during the first field cycle. After the second field cycle, f_{FM} decreases to 16.9% at zero field, which is very close to the zero-field f_{FM} value of 16.4% before the second field cycle. Consequently, the field-dependent neutron diffraction experiments reveal excellent reversibility of the $Mn_{1.15}Fe_{0.76}Mo_{0.04}P_{0.45}Si_{0.55}$ alloy, which is desirable for magnetic refrigeration applications driven by a cyclic magnetic field.

3.3. Magnetocaloric properties

For magnetic refrigeration applications, two primary thermodynamic parameters are of equal importance to the magnetocaloric materials, *i.e.*, the isothermal entropy change (Δs_T) and the adiabatic temperature change (ΔT_{ad}) [2]. The former measures the maximum amount of heat that can be taken from a load in one cooling cycle, while the latter determines the maximum temperature span between a load and a heat sink. From a practical perspective, magnetocaloric materials should have large reversible val-

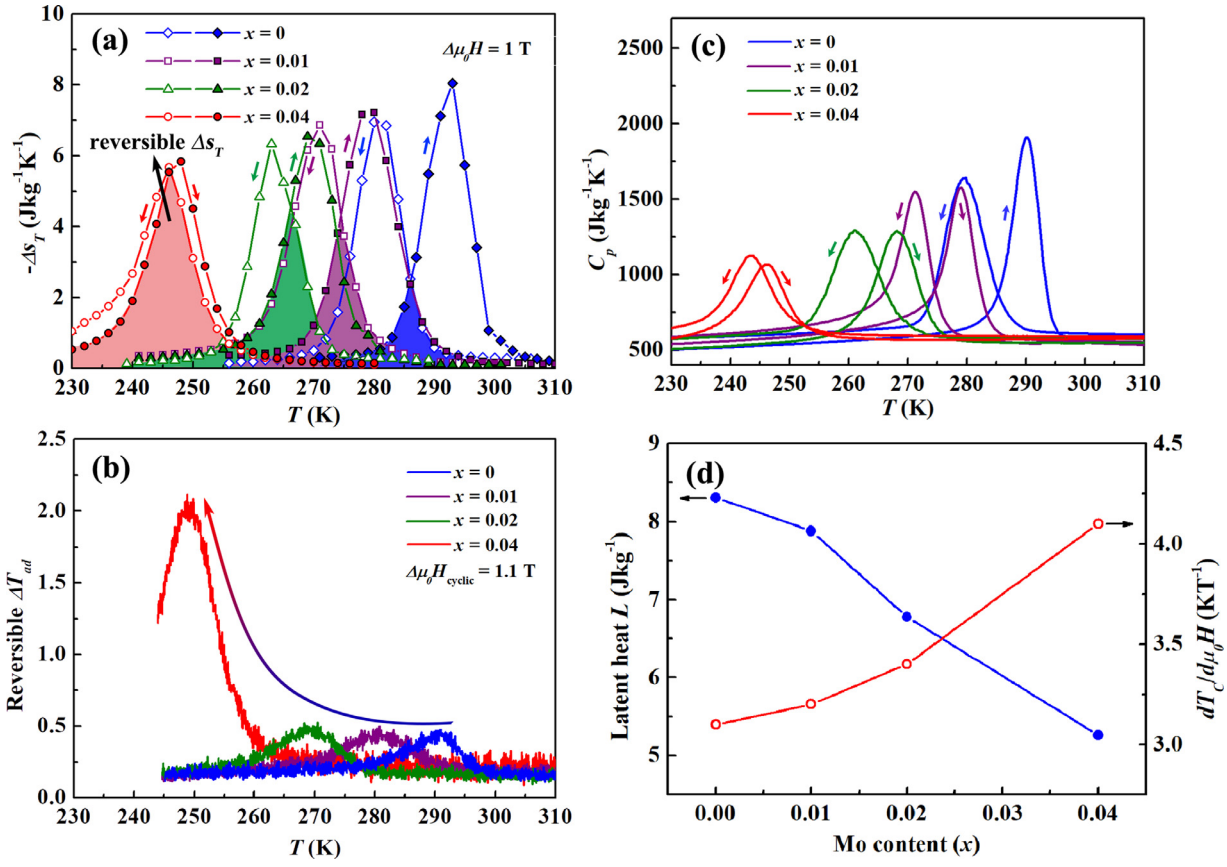

Fig. 3. (a) Isothermal entropy change in a field change of 1 T measured upon cooling (open symbols) and heating (solid symbols) for the $Mn_{1.15}Fe_{0.80-x}Mo_xP_{0.45}Si_{0.55}$ alloys. (b) Reversible adiabatic temperature change in a cyclic field of 1.1 T. (c) Specific heat at different temperatures (C_p-T curves) measured upon cooling and heating. (d) Latent heat derived from the C_p-T curves and the shift of T_C in a magnetic field ($dT_C/d\mu_0H$) derived from the M-T curves as a function of the Mo content.

ues in both Δs_T and ΔT_{ad} in small magnetic fields of about 1 T that can be generated by permanent magnets (*e.g.*, Nd-Fe-B).

The isothermal entropy change can be derived from isothermal magnetization measurements (as shown in Fig. 1(c) and (d)) based on Maxwell relations. It should be noted that the so-called "loop protocol" [51] was adopted in the isothermal magnetization measurements to avoid the thermal-history effect when a first-order phase transition is probed. Fig. 3(a) plots the temperature-dependent isothermal entropy change in a magnetic field change of 1 T for both cooling and heating processes of the $Mn_{1.15}Fe_{0.80-x}Mo_xP_{0.45}Si_{0.55}$ alloys. The reversible Δs_T can be estimated by the overlapped area between the cooling and heating branches of the Δs_T-T curves. The Mo-free alloy demonstrates a maximum Δs_T value of 8.0 J kg^{-1} K^{-1} in a field change of 1 T, while the maximum reversible Δs_T value drops to 2.5 J kg^{-1} K^{-1} due to the large irreversibility of the magnetoelastic transition. The reversible Δs_T is significantly increased with an increase in the Mo content, although the maximum Δs_T is slightly reduced. The $x = 0.04$ alloy shows a maximum reversible Δs_T value of about 5.5 J kg^{-1} K^{-1}, *i.e.*, approximately 91% of the maximum Δs_T is reversible in a magnetic field change of 1 T. Moreover, the maximum reversible Δs_T value of the $x = 0.04$ alloy is twice as large as that of the benchmark magnetocaloric material Gd [52].

The adiabatic temperature change associated with the magnetoelastic transition of the $Mn_{1.15}Fe_{0.80-x}Mo_xP_{0.45}Si_{0.55}$ alloys was directly measured by a Chromel-Constantan thermocouple in a homemade device [46,47] at Delft University of Technology. The reversible ΔT_{ad} at various temperatures is shown in Fig. 3(b). The Mo-free sample displays a maximum reversible ΔT_{ad} of only 0.4 K in a cyclic field of 1.1 T. The relatively small reversible ΔT_{ad} is attributed to the large thermal and magnetic hysteresis of the magnetoelastic transition, as shown in Fig. 1. The reversible ΔT_{ad} is significantly increased up to 2.0 K in the $x = 0.04$ sample, *i.e.*, 5 times as large as that of the Mo-free alloy.

The reversible ΔT_{ad} strongly depends on the shift of T_C in magnetic fields ($dT_C/d\mu_0H$), the transition width and the hysteresis [12, 53, 54]. The former two determine the upper limit of the ΔT_{ad}, while the latter affects the reversible part of the ΔT_{ad}. The $dT_C/d\mu_0H$ values derived from the M-T curves in different fields are 3.1, 3.2, 3.4 and 4.1 K T^{-1} for the $x = 0$, 0.01, 0.02 and 0.04 alloys, respectively, as shown in Fig. 3(d). According to the Clausius-Clapeyron description $dT_C/d\mu_0H = -T_C\Delta M/L$, the $dT_C/d\mu_0H$ is related to the transition temperature (T_C), the jump in magnetization (ΔM) and the latent heat (L) across the magnetoelastic transition. The T_C and ΔM both decrease with the Mo content (see Fig. 1(a)). The latent heat can be obtained from the integration of the temperature-dependent specific heat curves (*i.e.* the C_p-T curves shown in Fig. 3(c)), which decreases with an increase in the Mo content (see Fig. 3(d)). Therefore, the increase in the $dT_C/d\mu_0H$ after Mo substitution is predominantly due to the reduction of the latent heat, which benefits the maximum ΔT_{ad}. Although low thermal hysteresis of only 1 K is realized in the $x = 0.04$ alloy, the reversible ΔT_{ad} of 2.0 K is still much smaller than the shift of T_C (about 4.1 K) in a magnetic field of 1 T. This may be due to the large transition width across the magnetoelastic transition, which smears out the effect over a large temperature range [53,54]. Narrowing the transition width, *e.g.* via improving the compositional homogeneity and preparing textured samples [54,55], is expected to further improve the reversible ΔT_{ad} in the $(Mn,Fe)_2(P,Si)$-based magnetocaloric alloys.

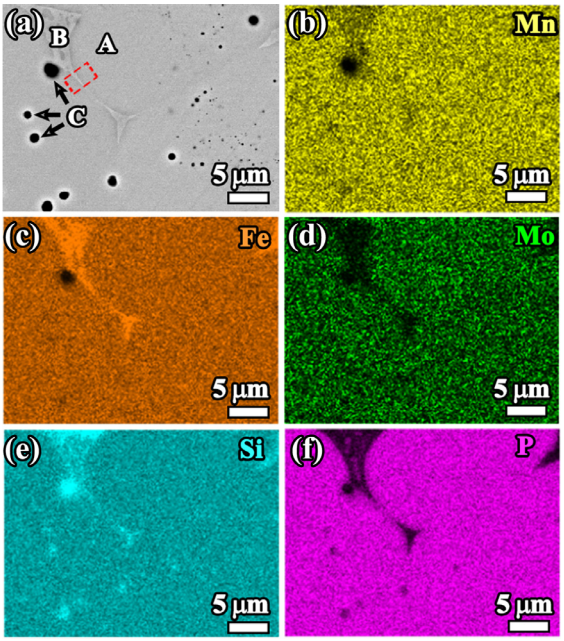

Fig. 4. (a) SEM BSE image and (b–f) the corresponding EDS maps of the $Mn_{1.15}Fe_{0.76}Mo_{0.04}P_{0.45}Si_{0.55}$ alloy.

3.4. Micro- and atomic-scale structural characterization

The magnetic and magnetocaloric results indicate that partial replacement of the Fe by Mo in the $Mn_{1.15}Fe_{0.80}P_{0.45}Si_{0.55}$ alloys leads to a remarkable enhancement in the reversibility of the magnetoelastic transition. To understand the underlying mechanism, we performed micro- and atomic-scale structural characterization using SEM and TEM. Fig. 4 shows the SEM backscattered electrons (BSE) image and the corresponding EDS maps of the $Mn_{1.15}Fe_{0.76}Mo_{0.04}P_{0.45}Si_{0.55}$ alloy. Based on the SEM and EDS results, three different phases can be identified in the alloy, *i.e.* the $(Mn,Fe)_2(P,Si)$ main phase (marked as "A" in the SEM image), the (Fe,Si)-rich grain-boundary phase (marked as "B") and the dispersed Si-rich phase (marked by "C"). Obviously, the Mo atoms enter the main phase instead of the impurity phases according to the EDS results (see Fig. 4(d)). It should be noted that the (Fe,Si)-rich grain-boundary phase and the dispersed Si-rich phase are present in all of the $Mn_{1.15}Fe_{0.80-x}Mo_xP_{0.45}Si_{0.55}$ (x = 0, 0.01, 0.02 and 0.04) samples, regardless of the Mo content.

We further performed TEM analyses on the $Mn_{1.15}Fe_{0.76}Mo_{0.04}P_{0.45}Si_{0.55}$ alloy. A region near the grain boundary (enclosed by the dashed lines in Fig. 4(a)) was lifted out for the TEM observations using a FIB system. Fig. 5(a) displays the bright-field TEM image of the selected region with corresponding EDS maps shown in Fig. 5(b–f). The Mo atoms are well distributed in the main phase, in good agreement with the SEM-EDS results. The concentration profiles across the grain boundary obtained from the EDS line-scan analysis (illustrated by the dashed arrow in Fig. 5(a)) are shown in Fig. 5(g). The average compositions of the main and the grain-boundary phases are $Mn_{1.08}Fe_{0.74}Mo_{0.03}P_{0.51}Si_{0.59}$ and $Fe_{1.34}Mn_{1.23}Si$, respectively, as derived from the EDS analysis. The measured composition of the main phase is close to the nominal composition despite the presence of a small amount of the Fe_3Si-type grain-boundary phase.

Fig. 5(h) and (i) displays the STEM-HAADF images taken along the [001] zone axis of the $(Mn,Fe)_2(P,Si)$ main phase and the [001] zone axis the Fe_3Si-type grain-boundary phase, respectively. No nano- or micro-cracks were observed at the phase interfaces, which suggests that the formation of the Fe_3Si-type grain-boundary phase does not deteriorate the structural integrity of the $(Mn,Fe)_2(P,Si)$ main phase. Enlarged views of the atomic arrangement of the main and the grain-boundary phases are shown in Fig. 5(j) and (k), respectively. The $(Mn,Fe)_2(P,Si)$ main phase retains the Fe_2P-type hexagonal structure (space group *P-62 m*) after the Mo substitution. No structural defects (*e.g.*, dislocations, stacking faults, twins) were detected in the $(Mn,Fe,Mo)_2(P,Si)$ main phase.

Consequently, the micro- and atomic-scale structural analyses reveal that the Mo atoms have entered the $(Mn,Fe)_2(P,Si)$ main phase, which causes subtle structural variations of the hexagonal unit cell and results in a remarkable improvement in the reversibility of the magnetoelastic transition.

3.5. In situ *temperature-dependent neutron diffraction studies*

The influence of the Mo substitution on the structure and magnetoelastic phase transition of the $(Mn,Fe)_2(P,Si)$ alloy was further investigated by *in situ* temperature-dependent neutron diffraction experiments. Fig. 6(a) and (b) shows the contour plots of the neutron diffraction patterns collected at different temperatures for the $Mn_{1.15}Fe_{0.80-x}Mo_xP_{0.45}Si_{0.55}$ alloys with x = 0 and 0.04, respectively. Both alloys exhibit discontinuous changes in the lattice parameters at the T_C, while the symmetry of the lattice is conserved. The higher intensity of the (001) peak at lower temperatures is due to the increased magnetic diffraction contribution. The magnetic and structural parameters of the $Mn_{1.15}Fe_{0.80-x}Mo_xP_{0.45}Si_{0.55}$ alloys can be derived from the Rietveld refinement of the neutron diffraction patterns (see Fig. 6(c) as an example). In the Fe_2P-type hexagonal structure (space group *P-62 m*), the Mn and Fe atoms prefer to occupy the 3 *g* and 3*f* crystallographic sites, respectively [56]. Our DFT calculations estimated the total energy of -576.2855 and −575.9443 eV for the structural configurations with the Mo atoms entering the 3 *g* and 3*f* sites, respectively, which predicts a preferential occupation of the Mo atoms at the 3 *g* site. Our neutron diffraction data experimentally verify the DFT prediction based on the large difference in the coherent neutron-scattering length between Mn (−3.73 fm), Fe (9.45 fm), and Mo (6.715 fm). The 3 *g* sites are occupied by the Mn (97.2%) and Mo (2.8%) atoms, while the 3*f* sites are occupied by the Fe (81.2%) and Mn (18.8%) atoms in the $Mn_{1.15}Fe_{0.76}Mo_{0.04}P_{0.45}Si_{0.55}$ alloy according to Rietveld refinement. In the Mo-free alloy, the Mn (3 *g* site) and Fe (3*f* site) moments derived from the neutron diffraction data are 2.55 ± 0.16 and 1.69 ± 0.16 μ_B, respectively, while those in the x = 0.04 alloy are 2.41 ± 0.16 and 1.65 ± 0.16 μ_B, respectively. Obviously, the non-magnetic Mo atoms entering the 3 *g* site slightly reduce the average sublattice magnetic moment at the 3 *g* site.

Fig. 6(d,e) shows the thermal-evolution of the lattice parameters for the $Mn_{1.15}Fe_{0.80-x}Mo_xP_{0.45}Si_{0.55}$ alloys. Note that the lattice parameters of the x = 0 and 0.04 alloys were derived from the Rietveld refinement of the temperature-dependent neutron diffraction data, while those of the x = 0.01 and 0.02 alloys were from the temperature-dependent X-ray diffraction data. All of the alloys show similar structural variations across the FM-to-PM transition, *i.e.* a decrease in lattice parameter *a* and an increase in lattice parameter *c*. With an increase in the Mo content, the relative changes in lattice parameters at the magnetoelastic transition are considerably reduced. For instance, the Mo-free alloy shows a relative change of 1.27% in lattice parameter *a* and a relative change of 2.73% in *c*, while the relative changes are significantly reduced to 0.79% and 1.71%, respectively in the x = 0.04 alloy. Consequently, the substitution of Fe by Mo in the $(Mn,Fe)_2(P,Si)$ alloys leads to improved structural compatibility between the PM and FM phases across the magnetoelastic transition.

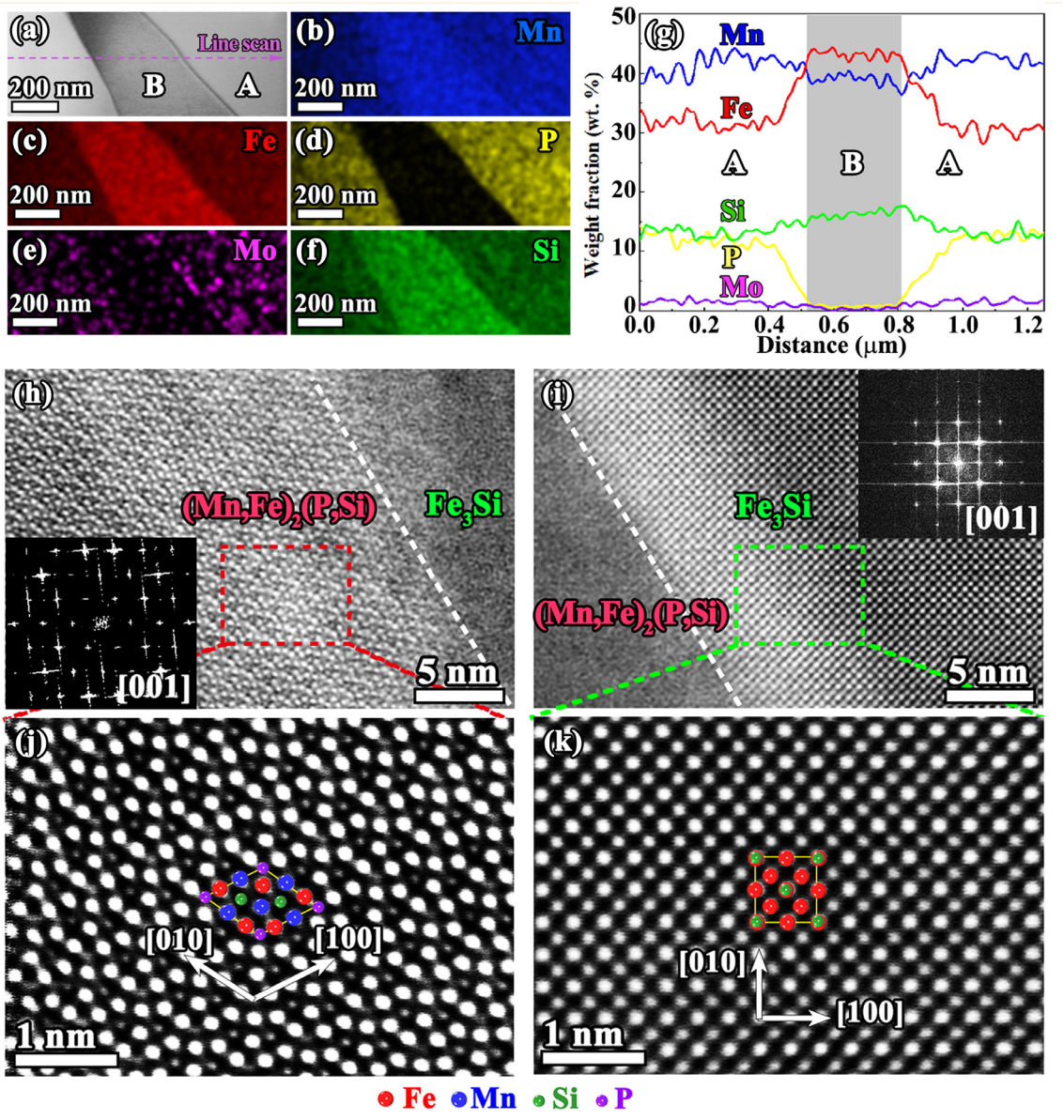

Fig. 5. (a) Bright-field TEM image and (b–f) the corresponding EDS maps for the $Mn_{1.15}Fe_{0.76}Mo_{0.04}P_{0.45}Si_{0.55}$ alloy. (g) Composition depth profile along the dashed lines in (a). STEM-HAADF images of the grain boundary area observed from (h) the [001] zone axis of the $(Mn,Fe)_2(P,Si)$ phase and (i) the [001] zone axis of the Fe_3Si-type phase. Insets in (h) and (i) are the corresponding FFT patterns of the $(Mn,Fe)_2(P,Si)$ and Fe_3Si-type phases, respectively. High-magnification STEM-HAADF images of (j) the $(Mn,Fe)_2(P,Si)$ main phase and (k) the Fe_3Si-type grain-boundary phase.

3.6. Mechanism of the enhanced reversibility

A higher structural compatibility between the parent and the product phases has been proven to exhibit a better reversibility of the martensitic transformation in NiTi-based shape memory alloys [23], NiMn-based Heusler alloys [24–26] and MnNiGe-based alloys [27]. The reduction in the thermal/magnetic hysteresis of the magnetoelastic transition in the $(Mn,Fe)_2(P,Si)$ alloys (see Fig. 1) can also be attributed to the improved structural compatibility after Mo substitution. Our previous neutron diffraction [42] and *in situ* TEM observations [16] revealed nucleation and growth processes of the magnetoelastic transition in the $(Mn,Fe)_2(P,Si)$ alloys. The large lattice mismatch between the PM and FM phases will induce considerable elastic strains in the material, which enhance the energy barrier for nucleation and hence increase the hysteresis of the magnetoelastic transition. The transition-induced elastic strain energy U_e can be calculated by

$$U_e = \frac{1}{2}\sum_{ij} C_{ij} e_i e_j \tag{1}$$

where the C_{ij} (i, j = 1,2,3,4,5,6) are the elastic constants and e_{ij} is the elastic strain. For a hexagonal system, the C_{ij} can be described by a matrix with five independent elements [57]:

$$C_{ij} = \begin{pmatrix} C_{11} & C_{12} & C_{13} & 0 & 0 & 0 \\ C_{12} & C_{11} & C_{13} & 0 & 0 & 0 \\ C_{13} & C_{13} & C_{33} & 0 & 0 & 0 \\ 0 & 0 & 0 & C_{44} & 0 & 0 \\ 0 & 0 & 0 & 0 & C_{44} & 0 \\ 0 & 0 & 0 & 0 & 0 & (C_{11}-C_{12})/2 \end{pmatrix} \tag{2}$$

The tensile strain within the *ab* plane is $e_1 = e_2 = \Delta a/a$ and along the *c* axis $e_3 = \Delta c/c$. Combining Eqs. (1), and (2) and neglect-

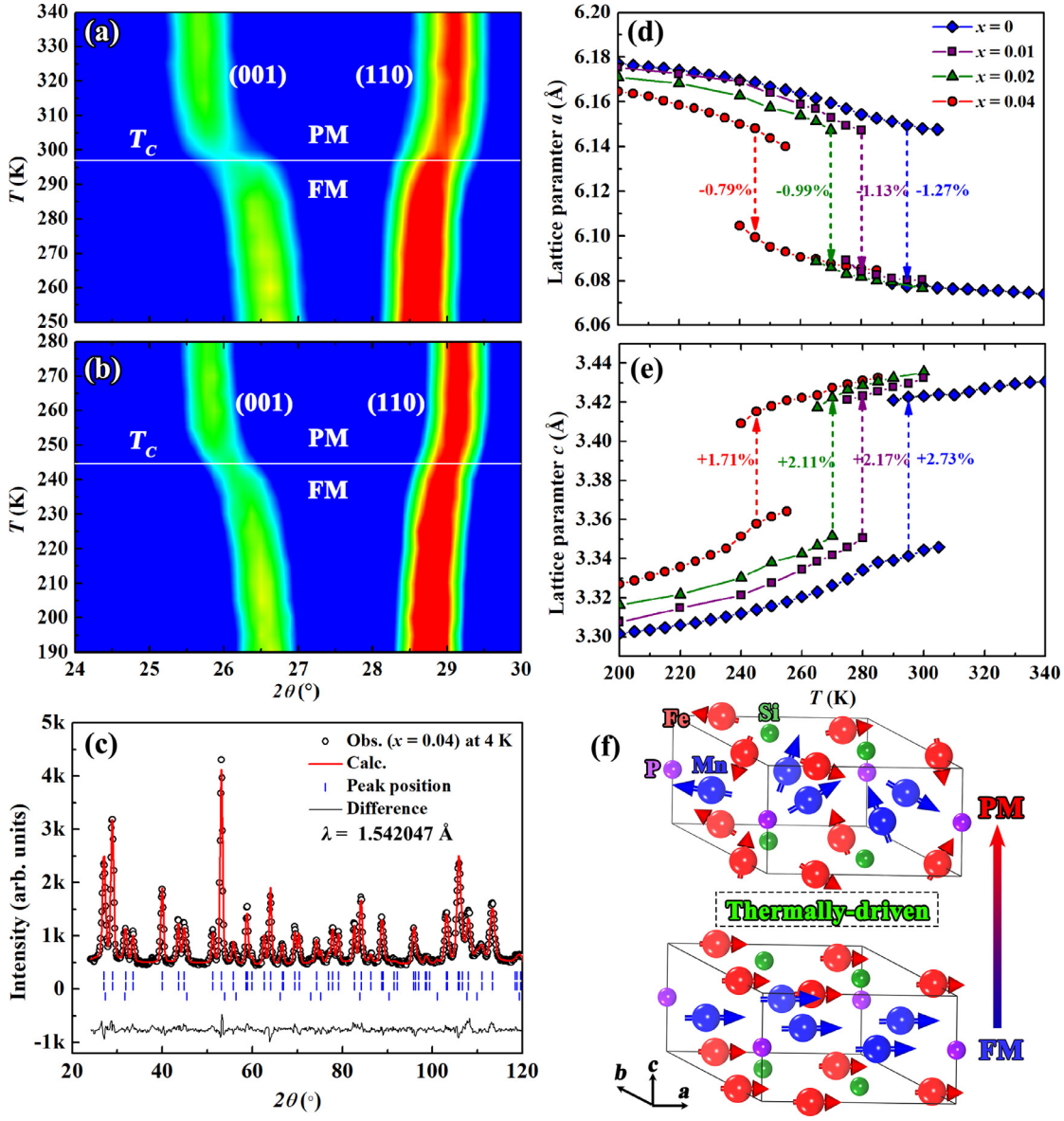

Fig. 6. Contour plots of the temperature-dependent neutron diffraction patterns for the $Mn_{1.15}Fe_{0.80-x}Mo_xP_{0.45}Si_{0.55}$ alloys with $x = 0$ (a) and 0.04 (b). (c) Rietveld refinement of the neutron diffraction pattern collected at $T = 4$ K in zero magnetic field for the $Mn_{1.15}Fe_{0.76}Mo_{0.04}P_{0.45}Si_{0.55}$ alloy. Vertical lines indicate the peak positions (from top to bottom) of the nuclear structure of the $(Mn,Fe)_2(P,Si)$ phase, the magnetic structure of the $(Mn,Fe)_2(P,Si)$ phase, and the Fe_3Si-type secondary phase, respectively. Thermal evolution of the lattice parameters a (d) and c (e) for the $Mn_{1.15}Fe_{0.80-x}Mo_xP_{0.45}Si_{0.55}$ alloys. Note that the lattice parameters of the $x = 0$ and 0.04 alloys were derived from temperature-dependent neutron diffraction patterns, while those of the $x = 0.01$ and 0.02 alloys were derived from temperature-dependent X-ray diffraction patterns. (f) Schematic illustration of the thermally-induced magnetoelastic transition in $(Mn,Fe)_2(P,Si)$ alloys.

ing the shear strains, the elastic strain energy U_e induced across the magnetoelastic transition of the $(Mn,Fe)_2(P,Si)$ alloys can be estimated by

$$U_e = (C_{11} + C_{12})e_1^2 + 2C_{13}e_1e_3 + \frac{1}{2}C_{33}e_3^2 \quad (3)$$

Taking the elastic constants reported by Roy et al. [58] and the elastic strain ($\Delta a/a$ and $\Delta c/c$ values at T_C) from Refs. [59–64], we can calculate the elastic strain energy U_e at T_C of the $(Mn,Fe)_2(P,Si)$ alloys with different compositions based on Eq. (3). Fig. 7 shows the relationship between the elastic strain energy and the thermal hysteresis for various $(Mn,Fe)_2(P,Si)$ alloys. This Ashby-like plot demonstrates that the thermal hysteresis of the $(Mn,Fe)_2(P,Si)$ alloys can be minimized by reducing the transition-induced elastic strain energy. This strategy may also be applicable to other magnetoelastic materials like $La(Fe,Si)_{13}$ [5,6], FeRh [65] and Eu_2In [66] since the elastic strain energy plays a similar role in the transition.

3.7. Mechanism of the tunable transition temperature

Giant MCE is usually observed in a narrow temperature range around the T_C of the magnetoelastic transition. To facilitate wide temperature spans in magnetic refrigerators, multi-layered regenerators have been proposed, which require stacks of magnetocaloric materials with gradually varying T_C values. The T_C of the $(Mn,Fe)_2(P,Si)$ alloys can easily be tuned via compositional variations, *e.g.* metal- and nonmetal-element substitution [61,67–70], as well as light element additions [46,71,72], which are desirable for fabricating multi-layered regenerators. However, the tuning mechanism of T_C in the $(Mn,Fe)_2(P,Si)$ alloys is still not well understood. High-resolution X-ray diffraction reveals an electron-density redis-

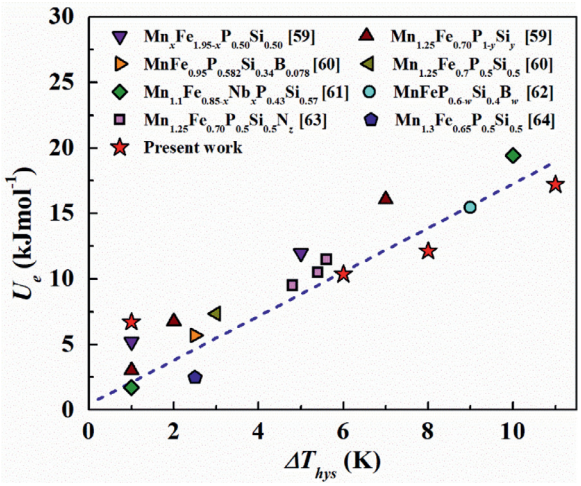

Fig. 7. Ashby-like plot demonstrating the relationship between the elastic strain energy U_e at T_C and the thermal hysteresis ΔT_{hys} for the $(Mn,Fe)_2(P,Si)$ alloys. The dashed line is a guide to the eyes.

tribution across the magnetoelastic transition of the $(Mn,Fe)_2(P,Si)$ alloys [73]. DFT calculations suggest a partial quenching of the Fe moment on the 3*f* site in addition to the order-disorder transition of the spin arrangement at the magnetoelastic transition [4,73]. Our temperature-dependent neutron diffraction in Fig. 6 indicates significant lattice distortions accompanying the magnetoelastic transition. Consequently, the magnetoelastic transition in the $(Mn,Fe)_2(P,Si)$ alloys is associated with strong electron-spin-lattice coupling.

In the $(Mn,Fe)_2(P,Si)$ alloys, the Fe-Si layer (*i.e.* the (001) lattice plane) and the Mn-P layer (*i.e.* the (002) lattice plane) are packed alternatively along *c* axis of the hexagonal structure. Fig. 8 presents the calculated ELF contour maps on the Fe-Si and Mn-P layers in the FM Fig. 8(a) and (b) and PM Fig. 8(c) and (d) states. Higher ELF values correspond to more localized electrons, suggesting a stronger covalent bonding between the neighboring atoms. A noticeable difference in the ELF values between the FM and PM states can be observed around both the Fe and Mn atoms. To quantitatively study the subtle variations in the covalent bonding across the FM-PM transition, Fig. 8(e) and (f) compares the line profiles of the ELF values between the PM and FM states. The most significant change in the ELF is found between the nearest Fe-Fe atoms, where the maximum ELF value in the PM state is 52.2% higher than that in the FM state. The maximum ELF values between the nearest Mn-Mn and Fe-Si atoms in the PM state are 20.8 and 5.1% higher than that in the FM state, respectively. Therefore, the ELF results suggest a significant enhancement of the covalent bonding between the neighboring atoms across the FM-to-PM transition, predominantly between the nearest Fe-Fe atoms.

The enhancement in the covalent bonding associates with a considerable shortening of the nearest Fe-Fe distance across the FM-to-PM transition, as shown in Fig. 9(a). Although the change in the Fe-Fe distance is slightly smaller than that in the Mn-Mn distance at the transition, the enhancement in the covalent bonding is more pronounced in the former. This may be due to the shorter Fe-Fe distances ($\approx$ 2.7 Å) compared to the Mn-Mn distances ($>$ 3.2 Å) in both FM and PM states, which leads to a stronger sensitivity of the Fe-Fe covalent bonding to the bond distance. The shorter Fe-Fe distance in the PM state may cause a larger overlap of the 3*d* orbitals between the neighboring Fe atoms, leading to a weaker exchange splitting between the majority and minority 3*d* band and hence a partial quenching of the Fe moment in the PM state. Consequently, the magnetoelastic transition in the $(Mn,Fe)_2(P,Si)$ alloys is dominated by the competition between the covalent bonding and the ferromagnetic exchange coupling. Rising the temperature of the system will boost thermal fluctuations and destroy the ferromagnetic exchange coupling between the neighboring moments, which favors the covalent bonding and thus the PM state. As a result, a thermally-driven magnetoelastic transition is observed in the $(Mn,Fe)_2(P,Si)$ alloys (illustrated in Fig. 6(f)). Alternatively, applying an external field will strengthen the ferromagnetic exchange coupling in the $(Mn,Fe)_2(P,Si)$ system, which favors the FM state and can thereby induce the magnetoelastic transition (illustrated in Fig. 2(b)).

Apart from the thermal and magnetic stimuli, the direct change of bond distance via compositional variations can also effectively manipulate the balance between covalent bonding and ferromagnetic exchange coupling. Here we take the Mo substitution for Fe as an example to elucidate the tuning mechanism of the T_C via compositional variations in the $(Mn,Fe)_2(P,Si)$ alloys. Fig. 10(a) shows the relationship between the T_C and the *c*/*a* ratio of the hexagonal structure for the $Mn_{1.15}Fe_{0.80-x}Mo_xP_{0.45}Si_{0.55}$ alloys. Note that the *c*/*a* ratio was derived from the Rietveld refinement of the neutron and X-ray diffraction data at 200 K, where all the samples were in the FM state. Interestingly, the T_C value decreases almost linearly with the *c*/*a* ratio of the FM phase, suggesting an underlying coupling between the structural parameters and the magnetic transition. Fig. 10(b–d) plots the nearest Fe-Fe, Fe-Si and Mn-Mn distances with respect to T_C. Obviously, the $Mn_{1.15}Fe_{0.80-x}Mo_xP_{0.45}Si_{0.55}$ alloy with a higher T_C corresponds to larger Fe-Fe, Fe-Si and Mn-Mn interatomic distances in the FM state. This can also be understood from the competition between covalent bonding and ferromagnetic exchange coupling. The covalent bonding is weakened with increasing interatomic distances, which stabilizes the FM state and thus pushes the T_C to higher temperatures. Tuning the T_C of the $(Mn,Fe)_2(P,Si)$ alloys via other metal- and nonmetal-element substitution [61,67–70], as well as light element addition [46,71,72] can also be explained by the competition between covalent bonding and ferromagnetic exchange coupling. The proposed tuning mechanism of the magnetoelastic transition is expected to be applicable to other magnetoelastic materials like $La(Fe,Si)_{13}$ [5, 6], FeRh [65] and Eu_2In [66], where the magnetoelastic transition is also dominated by the strong electron-spin-lattice coupling.

4. Conclusion

In summary, we found a significant enhancement of the reversible magnetocaloric properties in $(Mn,Fe)_2(P,Si)$ alloys by a partial substitution of Fe by Mo. Both the reversible adiabatic temperature change and the reversible isothermal entropy change are significantly increased in the $Mn_{1.15}Fe_{0.76}Mo_{0.04}P_{0.45}Si_{0.55}$ alloy, compared to the Mo-free alloy. To uncover the underlying mechanism of the enhanced reversible magnetocaloric properties, we performed comprehensive experimental (TEM and *in situ* neutron diffraction) and theoretical (DFT calculations) studies. *In situ* neutron diffraction in a cyclic magnetic field revealed a very small irreversible contribution ($\approx$ 5.3%) in the magnetoelastic transition of the $Mn_{1.15}Fe_{0.76}Mo_{0.04}P_{0.45}Si_{0.55}$ alloy. The high reversibility in the $Mn_{1.15}Fe_{0.76}Mo_{0.04}P_{0.45}Si_{0.55}$ alloy also manifests itself by a small thermal hysteresis of 1 K. Based on the relative changes in the lattice parameters across the magnetoelastic transition, we calculated the transition-induced elastic strain energy, which shows a generalized relationship with the thermal hysteresis in the $(Mn,Fe)_2(P,Si)$ family. The enhanced reversible magnetocaloric properties after the Mo substitution can be attributed to the reduced transition-induced elastic strain energy and the resultant high reversibility of the magnetoelastic transition. Additionally, the ELF results suggest a significant strengthening of the covalent bonding between the

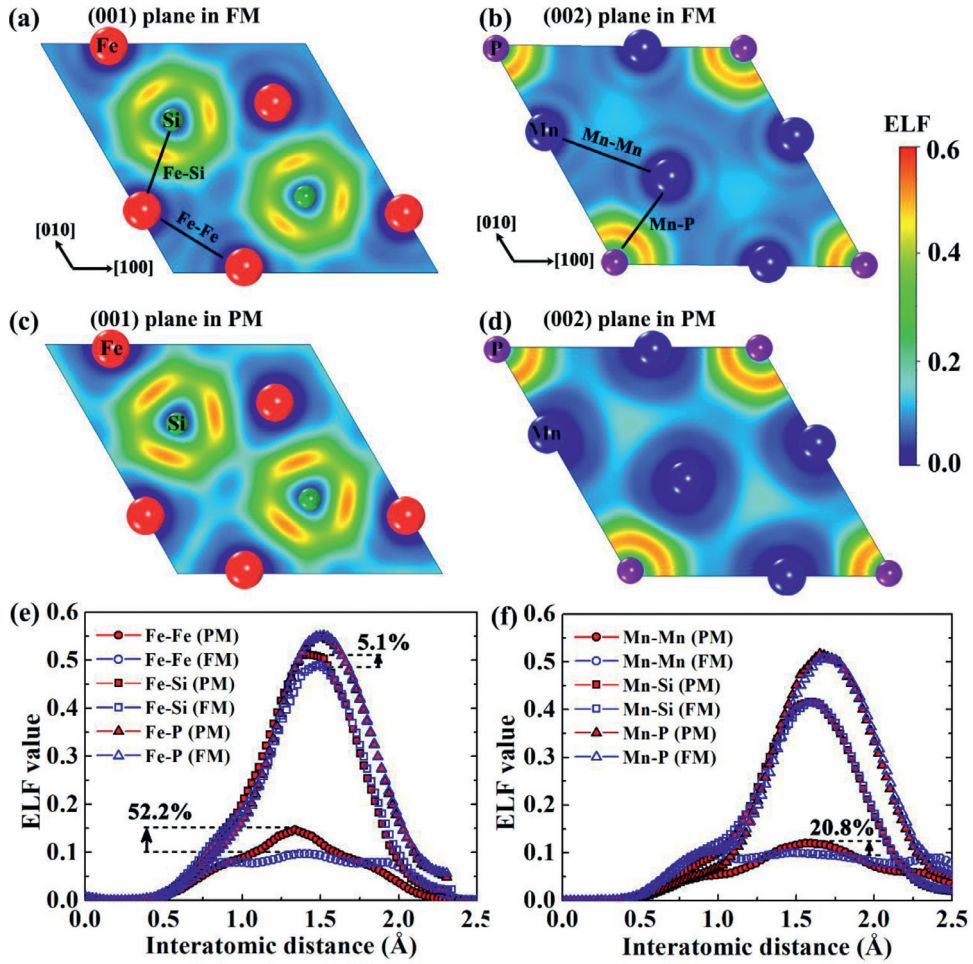

Fig. 8. Calculated ELF contour maps on the Fe-Si and Mn-P layers in (a, b) the FM and (c, d) the PM states of the $(Mn,Fe)_2(P,Si)$ alloys. Line profiles of the ELF values (e) between Fe and its nearest neighbors and (f) between Mn and its nearest neighbors. The stoichiometry of $MnFeP_{1/3}Si_{2/3}$ is assumed in the supercell for simplicity of the calculations.

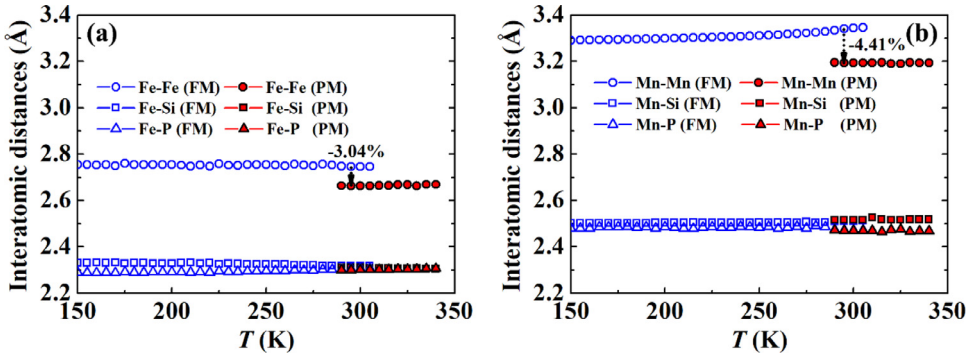

Fig. 9. Thermal evolution of interatomic distances extracted from neutron diffraction for the $Mn_{1.15}Fe_{0.80}P_{0.45}Si_{0.55}$ alloy. The errors on the refined distances are smaller than the symbol size.

nearest Fe-Fe atoms across the FM-to-PM transition, which is coupled to a partial quenching of the Fe moment as well as a shortening of the nearest Fe-Fe distance. Manipulating the magnetoelastic transition via the thermal and magnetic stimuli as well as compositional variations essentially relies on the tailoring of the strong electron-spin-lattice coupling in the $(Mn,Fe)_2(P,Si)$ alloys. The strategy for improving reversible magnetocaloric properties and the mechanism of tuning the magnetoelastic transition proposed in the present work are crucial to optimize the current material systems and to boost the search for promising magnetocaloric materials for magnetic refrigeration applications.

Acknowledgements

This work was supported by the National Natural Science Foundation of China (Nos. 51801102, U1832191, 12004179, and 11974184); the Natural Science Foundation of Jiangsu Province (Nos. BK20180491 and BK20180418); the Open Fund of Large

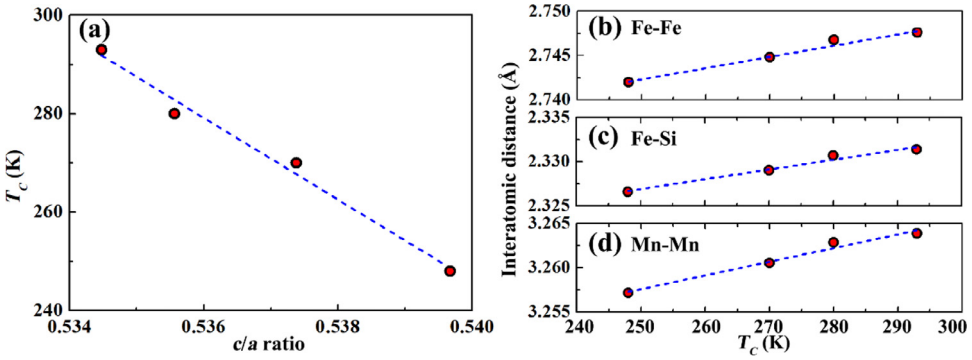

Fig. 10. (a) The relationship between the T_C of the FM-to-PM transition and the c/a ratio of the hexagonal structure at 200 K for the $Mn_{1.15}Fe_{0.80-x}Mo_xP_{0.45}Si_{0.55}$ alloys. (b–d) The nearest interatomic distances at 200 K to T_C. The errors on the c/a ratio and the interatomic distances are smaller than the symbol size.

Facilities in Nanjing University of Science and Technology; the Guangdong-Hong Kong-Macao Joint Laboratory for Neutron Scattering Science and Technology. This work is based on NPD experiments performed at Australian Nuclear Science and Technology Organization (ANSTO) in Australia with technical support of Dr. Chin Wei Wang. The authors thank Anton Lefering for the technical support on the adiabatic temperature change measurements. This work was carried out in the framework of the Joint Lab BiBer.

Reference

[1] A. Kitanovski, Adv. Energy Mater. 10 (2020) 1903741.
[2] T. Gottschall, K.P. Skokov, M. Fries, A. Taubel, I. Radulov, F. Scheibel, D. Benke, S. Riegg, O. Gutfleisch, Adv. Energy Mater. 9 (2019) 1901322.
[3] V.K. Pecharsky, K.A. Gschneidner Jr, Phys. Rev. Lett. 78 (1997) 4494–4497.
[4] N.H. Dung, Z.Q. Ou, L. Caron, L. Zhang, D.T.C. Thanh, G.A. de Wijs, R.A. de Groot, K.H.J. Buschow, E. Brück, Adv. Energy Mater. 1 (2011) 1215–1219.
[5] F.X. Hu, B.G. Shen, J.R. Sun, Z.H. Cheng, G.H. Rao, X.X. Zhang, Appl. Phys. Lett. 78 (2001) 3675–3677.
[6] A. Fujita, S. Fujieda, Y. Hasegawa, K. Fukamichi, Phys. Rev. B 67 (2003) 104416.
[7] E.K. Liu, W.H. Wang, L. Feng, W. Zhu, G.J. Li, J. Chen, H.W. Zhang, G.H. Wu, C.B. Jiang, H.B. Xu, F. de Boer, Nat. Commun. 3 (2012) 873.
[8] Y. Taguchi, H. Sakai, D. Choudhury, Adv. Mater. 29 (2017) 1606144.
[9] T. Krenke, E. Duman, M. Acet, E.F. Wassermann, X. Moya, L. Manosa, A. Planes, Nat. Mater. 4 (2005) 450–454.
[10] J. Liu, T. Gottschall, K.P. Skokov, J.D. Moore, O. Gutfleisch, Nat. Mater. 11 (2012) 620–626.
[11] T. Gottschall, K.P. Skokov, B. Frincu, O. Gutfleisch, Appl. Phys. Lett. 106 (2015) 021901.
[12] O. Gutfleisch, T. Gottschall, M. Fries, D. Benke, I. Radulov, K.P. Skokov, H. Wende, M. Gruner, M. Acet, P. Entel, M. Farle, Philos. Trans. R. Soc. A 374 (2016) 20150308.
[13] L.D. Landau, Zh. Eksp. Teor. Fiz. 7 (1937) 19–32.
[14] A.M.G. Carvalho, A.A. Coelho, S. Gama, F.C.G. Gandra, P.J. von Ranke, N.A. de Oliveira, Eur. Phys. J. B 68 (2009) 67–72.
[15] N.H. van Dijk, J. Magn. Magn. Mater. 529 (2021) 167871.
[16] X.F. Miao, H. Sepehri-Amin, K. Hono, Scr. Mater. 138 (2017) 96–99.
[17] M. Fries, L. Pfeuffer, E. Bruder, T. Gottschall, S. Ener, L.V.B. Diop, T. Gröb, K.P. Skokov, O. Gutfleisch, Acta Mater. 132 (2017) 222–229.
[18] A. Bartok, M. Kustov, L.F. Cohen, A. Pasko, K. Zehani, L. Bessais, F. Mazaleyrat, M. LoBue, J. Magn. Magn. Mater. 400 (2016) 333–338.
[19] K. Morrison, J. Moore, K. Sandeman, A. Caplin, L. Cohen, Phys. Rev. B 79 (2009) 134408.
[20] L. Morellon, Z. Arnold, C. Magen, C. Ritter, O. Prokhnenko, Y. Skorokhod, P.A. Algarabel, M.R. Ibarra, J. Kamarad, Phys. Rev. Lett. 93 (2004) 137201.
[21] H. Zhang, B.G. Shen, Z.Y. Xu, X.Q. Zheng, J. Shen, F.X. Hu, J.R. Sun, Y. Long, J. Appl. Phys. 111 (2012) 07A909.
[22] K. Bhattacharya, S. Conti, G. Zanzotto, J. Zimmer, Nature 428 (2004) 55–59.
[23] J. Cui, Y.S. Chu, O.O. Famodu, Y. Furuya, J. Hattrick-Simpers, R.D. James, A. Ludwig, S. Thienhaus, M. Wuttig, Z. Zhang, I. Takeuchi, Nat. Mater. 5 (2006) 286–290.
[24] Y.H. Qu, D.Y. Cong, S.H. Li, W.Y. Gui, Z.H. Nie, M.H. Zhang, Y. Ren, Y.D. Wang, Acta Mater. 151 (2018) 41–55.
[25] D.Y. Cong, L. Huang, V. Hardy, D. Bourgault, X.M. Sun, Z.H. Nie, M.G. Wang, Y. Ren, P. Entel, Y.D. Wang, Acta Mater. 146 (2018) 142–151.
[26] Y.H. Qu, D.Y. Cong, X.M. Sun, Z.H. Nie, W.Y. Gui, R.G. Li, Y. Ren, Y.D. Wang, Acta Mater. 134 (2017) 236–248.
[27] J. Liu, Y. Gong, Y. You, X. You, B. Huang, X. Miao, G. Xu, F. Xu, E. Brück, Acta Mater. 174 (2019) 450–458.
[28] C. Chluba, W. Ge, R. Lima de Miranda, J. Strobel, L. Kienle, E. Quandt, M. Wuttig, Science 348 (2015) 1004–1007.
[29] Y. Liu, X. Fu, Q. Yu, M. Zhang, J. Liu, Acta Mater. 207 (2021) 116687.
[30] V. Provenzano, A.J. Shapiro, R.D. Shull, Nature 429 (2004) 853–857.
[31] H. Sepehri-Amin, A. Taubel, T. Ohkubo, K.P. Skokov, O. Gutfleisch, K. Hono, Acta Mater. 147 (2018) 342–349.
[32] H. Hou, E. Simsek, T. Ma, N.S. Johnson, S. Qian, C. Cissé, D. Stasak, N. Al Hasan, L. Zhou, Y. Hwang, R. Radermacher, V.I. Levitas, M.J. Kramer, M.A. Zaeem, A.P. Stebner, R.T. Ott, J. Cui, I. Takeuchi, Science 366 (2019) 1116–1121.
[33] H. Chen, Y.D. Wang, Z. Nie, R. Li, D. Cong, W. Liu, F. Ye, Y. Liu, P. Cao, F. Tian, X. Shen, R. Yu, L. Vitos, M. Zhang, S. Li, X. Zhang, H. Zheng, J.F. Mitchell, Y. Ren, Nat. Mater. 19 (2020) 712–718.
[34] M. Trassinelli, M. Marangolo, M. Eddrief, V.H. Etgens, V. Gafton, S. Hidki, E. Lacaze, E. Lamour, C. Prigent, J.P. Rozet, S. Steydli, Y. Zheng, D. Vernhet, Appl. Phys. Lett. 104 (2014) 081906.
[35] R. Niemann, S. Hahn, A. Diestel, A. Backen, L. Schultz, K. Nielsch, M.F.X. Wagner, S. Fähler, APL Mater. 4 (2016) 064101.
[36] F.X. Hu, L. Chen, J. Wang, L.F. Bao, J.R. Sun, B.G. Shen, Appl. Phys. Lett. 100 (2012) 072403.
[37] A. Waske, L. Giebeler, B. Weise, A. Funk, M. Hinterstein, M. Herklotz, K. Skokov, S. Fähler, O. Gutfleisch, J. Eckert, Phys. Status Solidi RRL 9 (2015) 136–140.
[38] J. Lyubina, R. Schafer, N. Martin, L. Schultz, O. Gutfleisch, Adv. Mater. 22 (2010) 3735.
[39] E. Lovell, A.M. Pereira, A.D. Caplin, J. Lyubina, L.F. Cohen, Adv. Energy Mater. 5 (2015) 1401639.
[40] J.D. Moore, K. Morrison, K.G. Sandeman, M. Katter, L.F. Cohen, Appl. Phys. Lett. 95 (2009) 252504.
[41] Y. Liu, L.C. Phillips, R. Mattana, M. Bibes, A. Barthelemy, B. Dkhil, Nat. Commun. 7 (2016) 11614.
[42] X.F. Miao, L. Caron, J. Cedervall, P.C.M. Gubbens, P. Dalmas de Réotier, A. Yaouanc, F. Qian, A.R. Wildes, H. Luetkens, A. Amato, N.H. van Dijk, E. Brück, Phys. Rev. B 94 (2016) 014426.
[43] N.H. Dung, Moment formation and giant magnetocaloric effects in hexagonal Mn-Fe-P-Si compounds, Ph.D. dissertation, Delft University of Technology, Delft, 2012.
[44] A.J. Studer, M.E. Hagen, T.J. Noakes, Phys. B 385-386 (2006) 1013–1015.
[45] J. Rodriguez-Carvajal, Phys. B 192 (1993) 55–69.
[46] F. Guillou, G. Porcari, H. Yibole, N.H. van Dijk, E. Brück, Adv. Mater. 26 (2014) 2671.
[47] H. Yibole, F. Guillou, L. Zhang, N.H. van Dijk, E. Brück, J. Phys. D Appl. Phys. 47 (2014) 075002.
[48] G. Kresse, J. Furthmuller, Phys. Rev. B 54 (1996) 11169.
[49] A.D. Becke, K.E. Edgecombe, J. Chem. Phys. 92 (1990) 5397–5403.
[50] X.F. Miao, L. Caron, Z. Gercsi, A. Daoud-Aladine, N.H. van Dijk, E. Brück, Appl. Phys. Lett. 107 (2015) 042403.
[51] L. Caron, Z.Q. Ou, T.T. Nguyen, D.T. Cam Thanh, O. Tegus, E. Brück, J. Magn. Magn. Mater. 321 (2009) 3559–3566.
[52] K.A. Gschneidner, V.K. Pecharsky, A.O. Tsokol, Rep. Prog. Phys. 68 (2005) 1479–1539.
[53] K.G. Sandeman, Scr. Mater. 67 (2012) 566–571.
[54] F. Cugini, G. Porcari, S. Fabbrici, F. Albertini, M. Solzi, Philos. Trans. R. Soc. A 374 (2016) 20150306.
[55] T. Gottschall, D. Benke, M. Fries, A. Taubel, I.A. Radulov, K.P. Skokov, O. Gutfleisch, Adv. Funct. Mater. 27 (2017) 1606735.
[56] X.F. Miao, L. Caron, P. Roy, N.H. Dung, L. Zhang, W.A. Kockelmann, R.A. de Groot, N.H. van Dijk, E. Brück, Phys. Rev. B 89 (2014) 174429.
[57] J.F. Nye, Physical Properties of Crystals: Their Pepresentation By Tensors and Matrices, Oxford University Press, Oxford, UK, 1985.
[58] P. Roy, E. Torun, R.A. de Groot, Phys. Rev. B 93 (2016) 094110.
[59] N.H. Dung, L. Zhang, Z.Q. Ou, E. Brück, Scr. Mater. 67 (2012) 975–978.
[60] F. Guillou, H. Yibole, N.H. van Dijk, L. Zhang, V. Hardy, E. Brück, J. Alloys Compd. 617 (2014) 569–574.
[61] S.Y. Hu, X.F. Miao, J. Liu, Z.Q. Ou, M.Q. Cong, O. Haschuluu, Y.Y. Gong, F. Qian, Y.R. You, Y.J. Zhang, F. Xu, E. Brück, Intermetallics 114 (2019) 106602.
[62] M. Maschek, X. You, M.F.J. Boeije, D. Chernyshov, N.H. van Dijk, E. Brück, Phys. Rev. B 98 (2018) 224413.

[63] N.V. Thang, X.F. Miao, N.H. van Dijk, E. Brück, J. Alloys Compd. 670 (2016) 123–127.
[64] A. Pasko, A. Bartok, K. Zehani, L. Bessais, F. Mazaleyrat, M. LoBue, AIP Adv. 6 (2016) 056204.
[65] G. Shirane, R. Nathans, C.W. Chen, Phys. Rev. 134 (1964) A1547–A1553.
[66] F. Guillou, A.K. Pathak, D. Paudyal, Y. Mudryk, F. Wilhelm, A. Rogalev, V.K. Pecharsky, Nat. Commun. 9 (2018) 2925.
[67] J. Lai, B. Huang, X. Miao, N. Van Thang, X. You, M. Maschek, L. van Eijck, D. Zeng, N. van Dijk, E. Brück, J. Alloys Compd. 803 (2019) 671–677.
[68] Z.Q. Ou, N.H. Dung, L. Zhang, L. Caron, E. Torun, N.H. van Dijk, O. Tegus, E. Brück, J. Alloys Compd. 730 (2018) 392–398.
[69] H. Wada, K. Nakamura, K. Katagiri, T. Ohnishi, K. Yamashita, A. Matsushita, Jpn. J. Appl. Phys. 53 (2014) 063001.
[70] D. Liu, M. Yue, J. Zhang, T. McQueen, J. Lynn, X. Wang, Y. Chen, J. Li, R. Cava, X. Liu, Z. Altounian, Q. Huang, Phys. Rev. B 79 (2009) 014435.
[71] X.F. Miao, N.V. Thang, L. Caron, H. Yibole, R.I. Smith, N.H. van Dijk, E. Brück, Scr. Mater. 124 (2016) 129–132.
[72] Q. Zhou, Z.G. Zheng, W.H. Wang, L. Lei, A. He, D.C. Zeng, Intermetallics 106 (2019) 94–99.
[73] M.F.J. Boeije, P. Roy, F. Guillou, H. Yibole, X.F. Miao, L. Caron, D. Banerjee, N.H. van Dijk, R.A. de Groot, E. Brück, Chem. Mater. 28 (2016) 4901–4905.